Parasitic Wave Excitation by Multimode Coupling in a Raman-Regime Free-Electron Laser

Yasuaki Kishimoto, Hisako Oda,[a] and Makoto Shiho
Department of Thermonuclear Fusion Research, Naka Fusion Research Establishment, Japan Atomic Energy Research Institute, Naka Ibaraki 311-01, Japan
(Received 10 October 1989)

Mechanisms of parasitic wave excitation in a high-current Raman-regime free-electron laser (FEL) are investigated by use of a one-dimensional multimode FEL amplification code. It is found that multimode coupling among sideband waves and the primary wave plays an important role in the parasitic wave excitation in addition to the sideband instability. Such a multimode coupling process is observed in both the linear amplification stage and the nonlinear trapping stage, and modulates the output signal to a level comparable with that solely due to the sideband instability.

PACS numbers: 42.55.Tb

Analysis of parasitic wave excitation in the free-electron laser (FEL) is important for determining the quality of the output radiation signal. One of the important mechanisms of parasitic wave excitation is the sideband instability, where the periodic electron bounce motion (frequency Ω_B) in a ponderomotive potential well causes a wave instability shifted from the primary signal frequency. The sideband instability has been extensively studied analytically[1-3] and computationally[4,5] in the Compton regime, but rarely in the Raman regime. In the high-efficiency regime, Lin first investigated parasitic wave excitation by using the $1\frac{2}{2}$ electromagnetic particle code and found that waves shifted to the low-frequency side grow with a larger growth rate than that of the primary wave, as a result of the sideband instability.[6]

In this paper, we present a different type of excitation mechanism of parasitic waves in the Raman regime, in addition to the so-called sideband instability discussed in the literature.[1-6] The mechanism is due to multimode coupling among waves of different frequency, which generally exists in a system as a result of the sideband instability and the linear FEL amplification. Such multimode coupling is observed in both linear and nonlinear trapping stages and modulates the output signal to a level comparable with that solely due to the sideband instability.

Here we investigate the above phenomena by employing a one-dimensional helical-wiggler model in which the radiation and electrostatic fields are Fourier decomposed as

$$\mathbf{A}(z,t)=\sum_m A_m(z)(\mathbf{e}_x\cos\hat{\psi}_m-\mathbf{e}_y\sin\hat{\psi}_m)\,, \tag{1}$$

$$\Phi(z,t)=\sum_m \Phi_m(z)\cos\hat{\psi}_{em},\ \text{for } m=0,\pm1,\pm2,\ldots, \tag{2}$$

where $\hat{\psi}_m(z)=\int_0^z k_{+m}(z')dz'-\omega_m t+\theta_m$ and $\hat{\psi}_{em}(z)=\int_0^z k_m(z')dz'-\omega_m t+\theta_m$. $\omega_m/2\pi$ is the frequency of mode m ($\omega_{m=0}\equiv\omega_0$ denotes the primary wave), and k_{+m} and k_m are the corresponding wave numbers. θ_m is the initial electron phase.

We assume here that $\Delta\omega\equiv\omega_0/N$ (N an integer) is a minimum frequency difference between two adjacent modes. Therefore, the nonlinear driving current $J_{\rm NL}$ in Maxwell's equation has to be determined from the particle dynamics extended over a long interaction time length $\Delta T=2\pi/\Delta\omega$. Substituting $\mathbf{A}(z,t)$ and $\Phi(z,t)$ together with the microscopic current density into Maxwell's equation, we obtain non-wiggler-averaged field equations for slowly varying parts of mode m, $a_m\equiv eA_m/mc^2$ and $\phi_m\equiv e\Phi_m/mc^2$, as follows:

$$\frac{\partial^2 a_m}{\partial z^2}+\left(\frac{\omega_m^2}{c^2}-k_{+m}^2\right)a_m=\frac{\omega_b^2}{c^2}\left\langle\frac{\beta_{z0}}{v_z}(v_1\cos\psi_m-v_2\sin\psi_m)\right\rangle_m\,, \tag{3}$$

$$2k_{+m}^{1/2}\frac{\partial}{\partial z}(k_{+m}^{1/2}a_m)=-\frac{\omega_b^2}{c^2}\left\langle\frac{\beta_{z0}}{v_z}(v_1\sin\psi_m+v_2\cos\psi_m)\right\rangle_m\,, \tag{4}$$

$$\frac{\partial\phi_m}{\partial z}=-\frac{2\omega_b^2}{c\omega_m}\langle\beta_{z0}\sin\hat{\psi}_{em}\rangle_m\,, \tag{5}$$

$$k_m\phi_m=-\frac{2\omega_b^2}{c\omega_m}\langle\beta_{z0}\cos\hat{\psi}_{em}\rangle_m,\ \text{for } m=0,\pm1,\pm2,\ldots, \tag{6}$$

where $\beta_{z0}=v_{z0}/c$ [$v_{z0}\equiv v_z(t_0)$ is the initial axial velocity] and $\psi_m=\hat{\psi}_m+\int k_w\,dz$. v_1,v_2 denote the perpendicular components of an electron velocity described by the helical coordinate. An initial electron phase $\psi_{0m}\equiv-\omega_m t_0$ in $\hat{\psi}_m$ and $\hat{\psi}_{em}$ extends over $\{-\omega_m\pi/\Delta\omega,+\omega_m\pi/\Delta\omega\}$ and $\langle(\cdots)\rangle_m$ in Eqs. (3)-(6) represents an average with respect to ψ_{0m}. Equations (3)-(6) couple to $3N_T$ (N_T is the number of test particles) equations of electron motion uniformly distributed in phase space.

In the numerical calculation, a millimeter radiation field of $f=60$ GHz is injected as the primary radiation. A beam energy $E_b=1$ MeV ($\gamma_b\simeq2.96$), beam current density $I_b=1.5$ kA/cm^2, constant wiggler pitch

$\lambda_w (=2\pi/k_w)=4$ cm, and wiggler field $B_w \simeq 1.94$ kG are employed. The wiggler field adiabatically increases over the entry region $0 \leq z \leq 10\lambda_w$. The initial level of the electrostatic potential $\phi_m(z=0) = -2\omega_b^2 \langle \beta_{z0} \cos\hat{\psi}_{em} \rangle / c\omega_m(k_{+m}+k_w)$ is determined from the numerical error which corresponds to an initial setting of test particles in phase space.[7] In the paper, no axial beam energy spread and no axial guide field are assumed. Note that the parameters employed here belong to the strong-Raman-scattering regime.

We first present the two-wave case (i.e., the primary wave and a single sideband wave). Figure 1(a) shows typical spatial evolutions of radiation and space-charge fields for the $f=60$ GHz primary wave and the $f=40$ GHz sideband. The initial input powers at $z=0$ are chosen to be $P_{\text{in},f=40}=10^{-3}$ W/cm^2 as a noise and $P_{\text{in},f=60}=10^{3}$ W/cm^2. After saturation of the primary wave ($\hat{z}_{\text{sat}} \equiv z_{\text{sat}}/\lambda_w \simeq 16$), the $f=40$ GHz wave, which has no linear FEL amplification, grows exponentially by the sideband instability with a growth rate of $\Gamma_{40} \equiv d \ln a_{40}/dz \simeq 0.16$ cm^{-1}. The sideband wave overtakes the primary one at around $\hat{z} \simeq 36$ and then saturates. The averaged particle fraction trapped by the primary ponderomotive potential, $\langle \delta_{60} \rangle$, decreases from 75% to 52% after the sideband wave saturates. The saturation of the sideband wave originates from the particle trapping. Owing to the relation between the ponderomotive phase velocities, i.e., $v_{p40} \equiv \omega_{40}/(k_{+40}+k_w) < v_{p60} \equiv \omega_{60}/(k_{+60}+k_w)$, the power level of the primary wave does not significantly decrease even after the sideband wave overtakes the primary one.

The result for the $f=20$ GHz sideband case is shown in Fig. 1(b). The growth rate of the sideband measured from $\hat{z}_{\text{sat}} \simeq 16$ is smaller ($\Gamma_{20,a} \simeq 0.1$ cm^{-1}) than that of the $f=40$ GHz case [Fig. 1(a)]. This result indicates that the $f=20$ GHz wave is rather off resonant for the sideband instability compared with the $f=40$ GHz wave. Figure 1(b) also shows that the growth rate of the sideband instability changes at around $\hat{z} \simeq 35$ and gives a smaller value ($\Gamma_{20,b} \simeq 0.025$ cm^{-1}) for $\hat{z} \gtrsim 35$. Such a change is considered to be an effect of the longitudinal electrostatic interaction. That is, for $\hat{z}_{\text{sat}} \lesssim \hat{z} \lesssim 35$, the electrostatic force $f_{es} \equiv e\partial\Phi/\partial z$ prevents a harmonic electron bounce motion in the ponderomotive potential.[7,8] An irregular electron motion modulates the bounce frequency Ω_B and the related sideband instability. On the other hand, the electrostatic interaction leads to phase scrambling of bunched electrons, which reduces f_{es}. The reduction of f_{es} for $\hat{z} \gtrsim 35$ restores the harmonic electron motion and the corresponding growth rate of the sideband instability.[9] Therefore, the region $\hat{z}_{\text{sat}} \lesssim \hat{z} \lesssim 35$ is recognized as a relaxation layer of the electrostatic interaction.

The frequency spectrum of the sideband growth rate Γ_s is shown in Fig. 2. The linear growth rate besides the $f=60$ GHz primary wave is also illustrated. An asymmetric Γ_s spectrum, where the lower sidebands exhibit a strong instability, is obtained in accordance with theoretical indications.[2,3] The typical frequency shift from the primary wave, $\Delta\omega_{s,\max}/2\pi$, is about 20 GHz. Evaluating the bounce frequency by the use of the familiar relation $\Omega_B \simeq 2ck_w[a_w\langle a_{m=0}\rangle/(1+a_w^2)]^{1/2}$,[1,2] we estimate the frequency shift as $\Delta\omega_{s,\max}/2\pi \simeq k_{+m=0}\Omega_B/2\pi k_w \simeq 14$

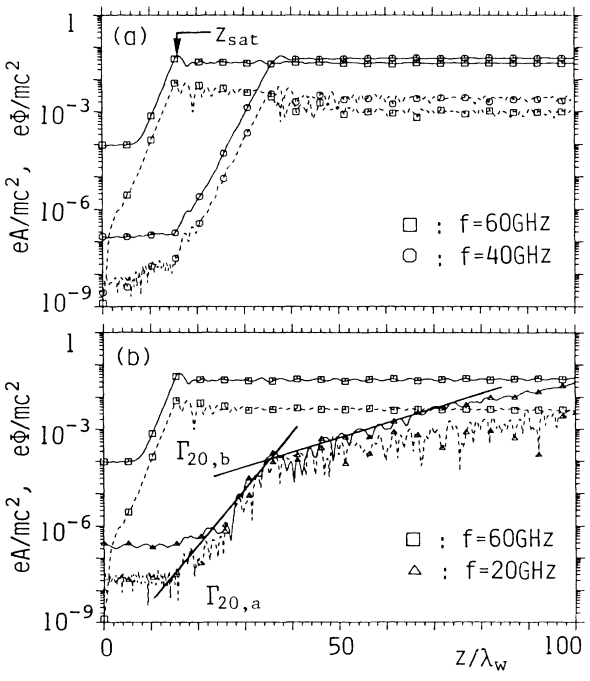

FIG. 1. Spatial evolution of the radiation field (solid line) and the space-charge field (dashed line) for (a) $f=40$ GHz and (b) $f=20$ GHz waves in the presence of the $f=60$ GHz primary wave with $P_{\text{in},60}=10^3$ W/cm^{-2}. $P_{\text{in}}=10^{-3}$ W/cm^{-2} is assumed for the sidebands.

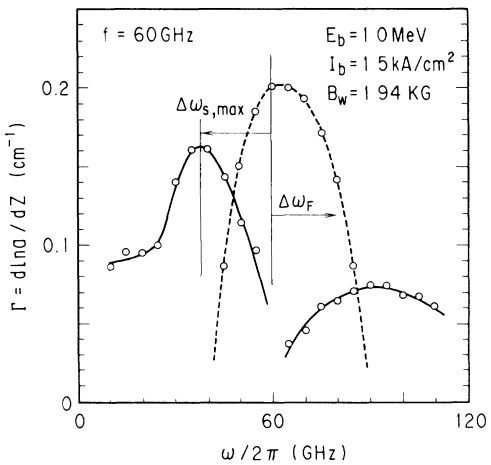

FIG. 2. Frequency spectrum of single-sideband instability in the presence of the $f=60$ GHz primary wave. The dashed line represents the linear FEL growth rate.

GHz by applying $a_w(=eB_w/mc^2k_w)=0.725$ and $\langle a_{m=0}\rangle \simeq 0.03$, which is roughly the same order as the numerical calculation. In Fig. 2, $\Delta\omega_F/2\pi \simeq 20$ GHz represents the typical frequency width for the primary wave.

Here, we develop the analysis to cases where multiple sideband waves exist. Figure 3(a) shows the result in which $f=40$ and 20 GHz sidebands are both included. It is found that the $f=20$ GHz wave grows following the growth rate of the $f=40$ GHz sideband, and shows a different feature from Fig. 1(b). This result is interpreted as follows: The beat field between the primary radiation field and the $f=40$ GHz sideband field induces a beam density modulation δn_e. δn_e can interchange energy with the $f=20$ GHz ponderomotive potential wave since δn_e propagates roughly with the phase velocity $v_{p20}\equiv\omega_{20}/(k_{+20}+k_w)$. As a result, amplification of the $f=20$ GHz parasitic wave takes place. Since the magnitude of the density modulation is proportional to the product of the two waves as[10]

$$a_{60}\exp[i(k_{+60}z-\omega_{60}t)+\Gamma_{60}z]\,a_{40}^{*}\exp[-i(k_{+40}z-\omega_{40}t)+\Gamma_{40}z],$$

the $f=20$ GHz wave has an exponential growth rate given by $\Gamma_{20}\simeq\Gamma_{60}+\Gamma_{40}\simeq\Gamma_{40}$, where $\Gamma_{60}\simeq 0$ is assumed for the saturation stage of the primary wave. The spatial evolution of the electron kinetic energy $W_k\equiv\sum_{j=1}^{N_T}(\gamma_j-1)/(\gamma_b-1)N_T$ is also illustrated in Fig. 3(b) to see the system energy conservation. The dashed line represents the single-sideband case of Fig. 1(a). It is found that the electron kinetic energy decreases considerably ($W_k\simeq 0.92\rightarrow 0.80$) when the sidebands grow and overtake the primary signal.

When an $f=80$ GHz field which has the FEL growth rate in the linear stage of the primary wave ($\Gamma_{60}\neq 0$) is injected with $P_{\mathrm{in},80}=1$ W/cm^2 in addition to the $f=40$ and 20 GHz fields, the behavior dramatically changes, as shown in Fig. 4: The $f=20$ and 40 GHz waves also grow exponentially in the linear stage. This result is also explained by the above-described mode-coupling scheme. That is, the coupling between the $f=60$ and 80 GHz waves induces the $f=20$ GHz wave with a growth rate given by $\Gamma_{20}\simeq\Gamma_{60}+\Gamma_{80}$. The $f=40$ GHz sideband wave is also induced through a second coupling between the $f=20$ and 60 GHz waves, with a higher growth rate $\Gamma_{40}\simeq\Gamma_{20}+\Gamma_{60}\simeq 2\Gamma_{60}+\Gamma_{80}$. Note that the wave growth rate becomes larger with an increasing number of mode couplings following the same additive law.[10]

When continuous-noise-spectrum radiation is present, such a multimode coupling process gives rise to an interesting result. Figure 5 shows the spatial evolution of the $f=60$ GHz primary wave with $P_{\mathrm{in},60}=10$ W/cm^2 with fourteen different-wavelength radiation fields from $f=10$ to 80 GHz (i.e., $\Delta\omega/2\pi=5$ GHz and $N\equiv\omega_0/\Delta\omega=12$), with $P_{\mathrm{in}}=10^{-3}$ W/cm^2, exist. In the linear stage ($8\lesssim\hat{z}\lesssim 18$), the $f=50$–80 GHz parasitic waves exhibit the linear FEL amplification (see Fig. 2). On the other hand, the $f=10$–45 GHz lower-frequency waves rapidly grow by multimode coupling. After saturation of the primary wave, the $f=40$ GHz wave, which has the maximum growth rate for the sideband instability, first overtakes the primary one at $\hat{z}\simeq 30$. The radiation power spectrum and the electron energy distribution at $\hat{z}=35$ are also illustrated in Fig. 5. Here we can see the radiation spectrum which corresponds to the linear FEL amplification and the sideband instability at around $f=60$ and 40 GHz, respectively. Furthermore, at around $f=20$ GHz, we observe a group of radiations induced by the mode coupling between the saturated pri-

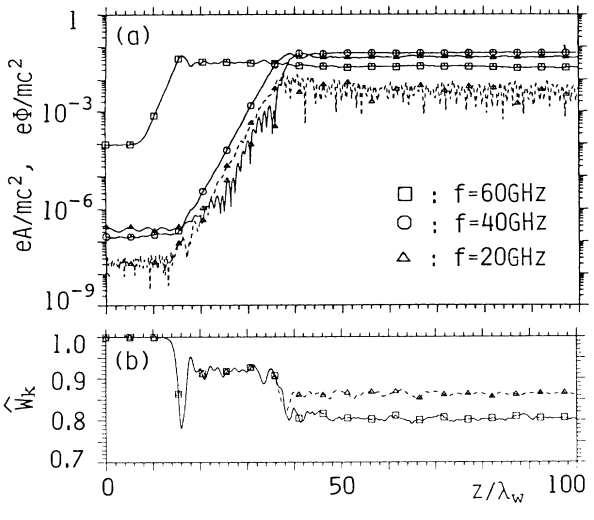

FIG. 3. (a) Spatial evolution of the radiation field for the $f=60$ GHz wave and $f=20$ and 40 GHz sidebands. The dashed line represents the space-charge field of the $f=20$ GHz wave. (b) Spatial evolution of the electron kinetic energy $\hat{W}_k$. The dashed line is the single-sideband case of Fig. 1(a).

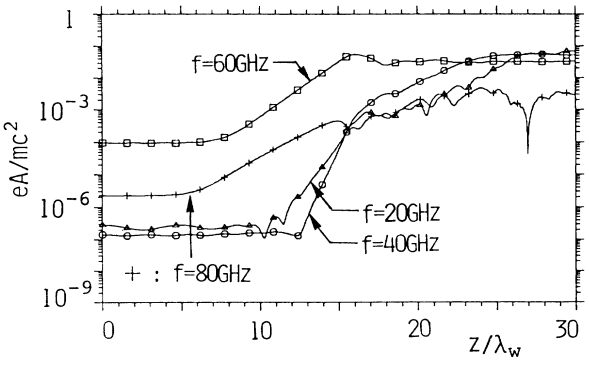

FIG. 4. Spatial evolution of radiation field for the $f=60$ GHz wave and $f=20$, 40 ($P_{\mathrm{in},20,40}=10^{-2}$ W/cm^2), and 80 GHz ($P_{\mathrm{in},80}=10^{-1}$ W/cm^2) sidebands.

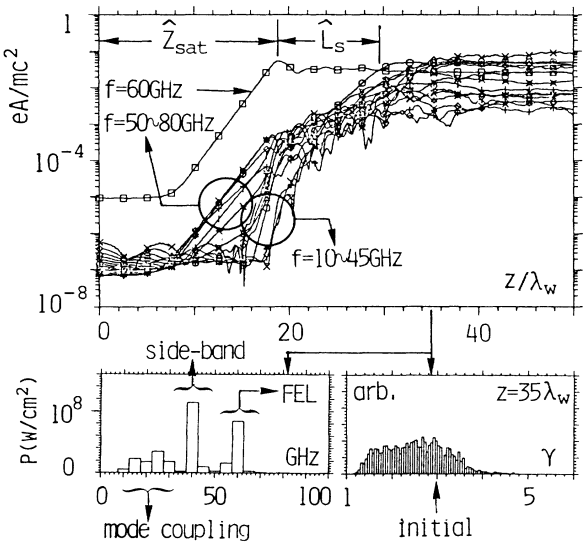

FIG. 5. Spatial evolution of the radiation power for the $f=60$ GHz ($P_{in,60}=10$ W/cm^2) wave and fourteen sidebands from $f=10$ to 80 GHz ($P_{in}=10^{-3}$ W/cm^2). The frequency spectrum and electron γ distribution at $\hat{z}=35$ are also shown.

mary wave and the sideband-instability waves ($f\simeq 40$ GHz). The center frequency of that spectrum ($f\simeq 20$ GHz) coincides with $f\simeq\Delta\omega_{s,max}/2\pi$ and the half-width is nearly equal to that of the sideband instability. The beam energy has also spread a great deal to the lower γ region. Note that the total power of the radiation spectrum induced by the mode coupling (10 GHz$\lesssim f\lesssim$30 GHz) is at the same level as that due to the linear FEL amplification and the sideband instability.

In Fig. 5, the wiggler length $\hat{L}_s\equiv L_s/\lambda_w\simeq 11$ is an important parameter for a realistic FEL design, because $\hat{L}_s$ represents a typical length over which the quality of the radiation field and the electron energy distribution significantly change. The trapped particle fraction $\langle\delta_{60}\rangle$ also decreases to 30% for $\hat{z}>\hat{z}_{sat}+\hat{L}_s$, although $\langle\delta_{60}\rangle\simeq 75\%$ for $\hat{z}<\hat{z}_{sat}+\hat{L}_s$. Here, the characteristic length $\hat{L}_s$ relates closely to the ratio of the initial powers of the parasitic noise field and of the primary one, i.e., $\alpha\equiv P_{in,noise}/P_{in,primary}$. With an increase of α (i.e., $\alpha\rightarrow 1$), L_s becomes close to zero, $L_s\rightarrow 0$, and a signal with a rather broad frequency spectrum is obtained. On the other hand, to obtain a monochromatic signal ($P_{40}/P_{60}\lesssim 10^{-1}$) for a fixed wiggler length of, for instance, $\hat{L}\simeq 24$, $\alpha\lesssim 10^{-3}$ is required. In the case of a tapered-wiggler FEL, the starting point of the tapering $\hat{z}_{tap}$ should be carefully chosen so as to satisfy the condition $0\lesssim\hat{z}_{tap}-\hat{z}_{sat}\lesssim\hat{L}_s$, since the trapped particle fraction $\langle\delta_{60}\rangle$ rapidly decreases for $\hat{z}\gtrsim\hat{z}_{sat}+\hat{L}_s$.

Finally, the multimode coupling described here significantly modulates the output radiation spectrum when $\Delta\omega_{s,max}\sim\Delta\omega_{FEL}\sim(\frac{1}{4}-\frac{1}{2})\omega_0$ (Ref. 11) is roughly satisfied. When $\Delta\omega_{s,max}$, $\Delta\omega_{FEL}\ll\omega_0$, the lower-frequency wave ($\omega\sim\Delta\omega_{s,max}$) induced by the mode coupling will saturate in a lower level since the phase velocity of that wave, i.e., $\Delta\omega_{s,max}/(k_{+s,max}+k_w)$, is too low to cause the separatrix to overlap with the sideband instability wave. In this paper, we employed a one-dimensional model which does not include waveguide effects. The excitation of lower-frequency parasitic waves may be suppressed by adjusting the waveguide dimension so as to satisfy the condition $\Delta\omega_{s,max}\lesssim\omega_c$, where ω_c is the cutoff frequency of the waveguide.

We are grateful to Dr. H. Maeda, Dr. S. Tokuda, Dr. T. Takeda, and Dr. M. Tanaka for their continuous encouragement.

[a]Permanent address: Kanazawa Computer Service Corp., Tokai, Naka, Ibaraki 319-11, Japan.

[1]N. M. Kroll, P. L. Moton, and M. N. Rosenbluth, IEEE J. Quantum Electron. **17**, 1436 (1981).

[2]R. C. Davidson and J. S. Wurtele, Phys. Fluids **30**, 557 (1987).

[3]S. R. Riyopoulos and C. M. Tang, Phys. Fluids **31**, 1708 (1988).

[4]D. C. Quimby, J. M. Slater, and J. P. Wilcoxon, IEEE J. Quantum Electron **21**, 979 (1986).

[5]B. Hafizi, A. Ting, P. Sprangle, and C. M. Tang, Phys. Rev. A **38**, 197 (1988).

[6]A. T. Lin, Phys. Rev. Lett. **46**, 1515 (1981).

[7]Y. Kishimoto, H. Oda, M. Shiho, K. Odajima, and H. Maeda, J. Phys. Soc. Jpn. **59**, 118 (1990).

[8]The ratio between f_{es} and the ponderomotive force f_p is estimated for the primary wave to be

$$|f_{es}/f_p|=2\xi^2\gamma^2k_w^2c\langle\delta\rangle|H(\psi,\psi_e)|/a_wa_m=_0\omega(k_++k_w),$$

where $\xi\equiv\omega_b/\gamma_b^{1/2}ck_w$, and $H(\psi,\psi_e)$ denotes the phase factor given by $H=\langle\beta_{z0}\cos\psi_e\rangle(\sin\psi_e/\sin\psi)$ (Ref. 7). From the above relation, we estimate the ratio as $|f_{es}/f_p|=0.5$–1.5 for $20\lesssim\hat{z}\lesssim 30$.

[9]$\Gamma_{20,a}$ tends to $\Gamma_{20,b}$ in the range $\hat{z}_{sat}\lesssim\hat{z}\lesssim 35$ by introducing the axial beam energy spread $\Delta\gamma_b$ which reduces f_{es} through a reduction of $H(\psi,\psi_e)$ in Ref. 8.

[10]A. A. Galeev and R. S. Sagdeev, *Reviews of Plasma Physics* (Consultants Bureau, New York, 1979), Vol. VII.

[11]In Lin's results (Ref. 6), this condition does not seem to be satisfied and this is considered to be one of the reasons why Ref. 6 does not observe the mode-coupling process described in this paper.